Mon. Not. R. Astron. Soc. **000**, 1–?? (2014) Printed 20 February 2014 (MN LATEX style file v2.2)

The X-ray Properties of Weak Lensing Selected Galaxy Clusters

P. A. Giles[1⋆], B. J. Maughan,[1] T. Hamana[2], S. Miyazaki[2], M. Birkinshaw,[1] R. S. Ellis[3], R. Massey[4]

[1] *HH Wills Physics Laboratory, University of Bristol, Tyndall Avenue, Bristol, BS8 1TL, UK*
[2] *National Astronomical Observatory of Japan, Mitaka, Tokyo 181-8588, Japan*
[3] *Astronomy Department, MS 249-17, California Institute of Technology, Pasadena, CA 91125, USA*
[4] *Institute of Computational Cosmology, Durham University, South Road, Durham DH1 3LE, UK*

18 February 2014

ABSTRACT

We present the results of an X-ray follow-up campaign targeting 10 Weak Lensing (WL) selected galaxy clusters from a *Subaru* WL survey. Eight clusters were studied with dedicated *Chandra* pointings, whereas archival X-ray data were used for the remaining two clusters. The WL clusters appear to fit the same scaling relation between X-ray luminosity and temperature as X-ray selected clusters. However, when we consider the luminosity-mass relation, the WL selected clusters appear underluminous by a factor 3.9±0.9 (or, alternatively, more massive by 2.9±0.2), compared to X-ray selected clusters. Only by considering various observational effects that could potentially bias WL masses, can this difference be reconciled. We used X-ray imaging data to quantify the dynamical state of the clusters and found that one of the clusters appears dynamically relaxed, and two of the clusters host a cool core, consistent with Sunyaev-Zel'dovich effect selected clusters. Our results suggest that regular, cool core clusters may be over-represented in X-ray selected samples.

Key words: Galaxies: clusters: general – Cosmology: observations – X-rays: galaxies: clusters – Gravitational lensing

1 INTRODUCTION

Clusters of galaxies are the largest gravitationally-collapsed structures in the Universe. The study of their number density and growth from high density perturbations in the early Universe offers insight into the underlying cosmology (e.g., Mantz et al. 2008; Vikhlinin et al. 2009b). However, the use of clusters as a cosmological probe requires an efficient method to find clusters over a wide redshift range, an observational method of determining the cluster mass and a method to compute the selection function or the survey volume in which clusters are found (Mantz et al. 2008). A variety of observational techniques has been brought to bear on these requirements, each with different strengths and weaknesses.

Early samples of clusters were based upon optical selection, however these samples have traditionally suffered from projection effects and uncertainties in the optical richness-mass relation. Recently, the first clusters have been detected in blind surveys using the Sunyaev-Zel'dovich effect (SZE; Staniszewski et al. 2009; Vanderlinde et al. 2010; Planck Collaboration et al. 2011a). This method holds much promise due to the redshift independence of the SZE (Birkinshaw 1999), however the use of the SZE as a mass estimator remains largely untested. Until now, the most effective method of building large, well defined cluster samples has been via X-ray selection. The high X-ray luminosities of clusters makes it relatively easy to detect and study clusters out to high redshifts, and X-ray cluster studies have provided a means to impose tight constraints on cosmological parameters (e.g. Vikhlinin et al. 2009b; Mantz et al. 2010b).

A common weakness of the three techniques outlined above is that the clusters are selected based on the properties of their minority baryonic content. However, cosmological constraints from those clusters are based on their masses, dominated by dark matter. This gives rise to complications both in the estimation of cluster masses (which must be inferred from the observed baryon properties) and in the determination of sample selection functions. Incorporating selection functions in any cosmological model depends crucially on the form and scatter of the relationship between

⋆ E-mail: P.Giles@bristol.ac.uk

the observable used to detect the cluster, and the cluster mass.

In principle, these complications may be avoided by defining cluster samples through gravitational lensing, the most direct observational probe of cluster masses. The development of weak lensing (abbreviated WL throughout) techniques has enabled the detection of clusters via the distortions of background galaxy shapes leading to the construction of WL selected cluster surveys. These include the Deep Lens Survey (Wittman et al. 2006) and our *Subaru* Weak Lensing Survey (Miyazaki et al. 2007), both $\approx$20 deg^2, and the large ($\sim$170 deg^2) CFHT Legacy Survey (Shan et al. 2012). However, while WL techniques are free from assumptions about the relationship between baryonic and dark matter in clusters, they are susceptible to the possibility of projection of multiple structures along the line of sight, leading to overestimates of cluster masses or false detections.

This paper aims to determine the X-ray properties of clusters detected via their WL signal. By constructing scaling relations based on the measured X-ray properties, we will determine whether the clusters follow simple scaling theory, which is a key ingredient in the determination of cosmological parameters. One of the most important measurements for use in cosmological studies is that of the cluster' mass. Much work has been done to determine cluster masses from weak lensing observations, and the comparison to X-ray observables and X-ray determined masses, however this is primarily based on X-ray selected cluster samples (e.g. Hoekstra 2007; Okabe et al. 2010b; Jee et al. 2011; Israel et al. 2012; Hoekstra et al. 2012; Mahdavi et al. 2013; Israel et al. 2014). We will compare the scaling relation between the X-ray luminosity and WL mass from WL selected and X-ray selected samples. The derivation of the WL cluster mass assumes that the clusters follow spherical symmetry. We investigate this assumption and determine the dynamical state and cool-core fraction of WL selected clusters.

The outline of this paper is as follows. In § 2 we discuss the sample selection and data reduction. The derivation of the cluster properties is given in § 3. In § 4 we present the results of our X-ray analysis and derive scaling relations. Our discussions and conclusions are presented in § 5 and § 6 respectively. Throughout this paper we assume a cosmology with $\Omega_{\rm M}$=0.3, Ω_Λ=0.7 and H_0=70 km s^{-1} Mpc^{-1}.

2 SAMPLE AND DATA REDUCTION

Our clusters were selected from the *Subaru* WL survey of Miyazaki et al. (2007). The sample defined in this work was constructed based upon confirmed cluster identification from spectroscopic follow up (Hamana et al. 2009). For 36 WL cluster candidates 15-32 galaxy redshifts were obtained per cluster, with 28 candidates securely identified as clusters. 10 of these clusters (within the redshift range $0.14 \leq z \leq 0.42$) were defined as a "clean" subset of clusters whose velocity dispersion could be evaluated from at least 12 spectroscopic member galaxies, and whose WL mass estimates are not affected by a neighboring system or field boundary. A summary of the 10 clusters investigated in this paper is given in Table 1. For eight of the clusters in the sample we obtained dedicated *Chandra* pointings, whereas SLJ1000.7 was observed in the COSMOS field with *Chandra* and SLJ0225.7 was observed in the XMM_LSS_13 field with *XMM*. We note however that the *Chandra* of SLJ1647.7 produced low quality data, we therefore chose to use an archived *XMM* observation for the analysis of this cluster.

For the eight clusters analysed using *Chandra* observations we used the CIAO[1] 4.4 software package with CALDB[2] version 4.4.7 and followed standard reduction methods. Since all observations were telemetered in VFAINT mode additional background screening was applied[3]. We inspected background light curves of the observations following the recommendations given in Markevitch et al. (2003), to search for possible background fluctuations. None of the observations were affected by periods of background flaring.

In order to take the background into account, we follow the method described in Vikhlinin et al. (2006). Briefly, *Chandra* blank-sky backgrounds were obtained, processed identically to the cluster, and reprojected onto the sky to match the cluster observation. We then renormalise the background in the 9.5–12 keV band, where the *Chandra* effective area is nearly zero and the observed flux is due entirely to the particle background events. Finally, to take into account differing contributions from the soft X-ray background, the spectra were subtracted and residuals were modeled in the 0.4-1keV band using an unabsorbed APEC thermal plasma model (Smith et al. 2001) with a temperature of 0.18 keV. This model was included in the spectral fitting for the cluster analysis.

The clusters SLJ0225.7 and SLJ1647 were observed by *XMM*. We used the Science Analysis Software (SAS) version 12.0.1 and the most recent calibration products as of Oct. 2013 for the analysis of these clusters.

Table 1 lists the total cleaned exposure times for each cluster.

3 CLUSTER PROPERTIES

In this section we outline the methods used to determine the cluster properties of our sample. Where possible we use the method outlined in Section 3.1, however for clusters with low SNR data, the properties are determined using one of the methods described in Section 3.2. Table 1 lists the analysis method used for each cluster.

3.1 The "Standard" Method

To determine the cluster properties of our sample we followed the procedures outlined in Maughan et al. (2012), for the *Chandra* observations. We detail our analysis for the *XMM* observations of the clusters SLJ0225.7 and SLJ1647.7 in Sect. 3.3.1 and 3.3.6 respectively. Briefly, cluster spectra were extracted and fits performed in the 0.6 - 9.0 keV band with an absorbed APEC model, with the absorbing column fixed at the Galactic value (Kalberla et al. 2005). We note that due to the low SNR of five of the clusters (see 3.3), the abundance was fixed at $0.3Z_\odot$ throughout this analysis. We determine the gas density profile for each cluster by converting the observed surface brightness profile (constructed

[1] See http://cxc.harvard.edu/ciao/
[2] See http://cxc.harvard.edu/caldb/
[3] See http://cxc.harvard.edu/ciao/why/aciscleanvf.html

Table 1. Basic properties of the cluster sample. Columns: (1) = Source name; (2) = ObsID of the observation (4/5 digits *Chandra*, 10 digits *XMM*); (3) = Right Ascension at J2000 of the WL peak (Hamana et al. 2009); (4) = Declination at J2000 of the WL peak (Hamana et al. 2009); (5) = Redshift of the cluster as determined from the *Subaru* spectroscopic follow-up (Hamana et al. 2009); (6) Cleaned exposure time; (7) Refers to the analysis method used to determine the properties of the cluster (see §3). † cluster observed with *XMM*.

Cluster	ObsID	RA	DEC	z	Exposure (ks)	Analysis
SLJ0225.7–0312†	0553910201	02 25 43.2	–03 12 36	0.1395	12	Low SNR(b)
SLJ1647.7+3455†	0652400401,12303	16 47 47.5	+34 55 13	0.2592	13	Low SNR(b)
SLJ0850.5+4512	12305	08 50 31.7	+45 12 12	0.1935	29	Standard
SLJ1000.7+0137	8022,8023,8555	10 00 45.5	+01 39 26	0.2166	98	Standard
SLJ1135.6+3009	12302	11 35 38.4	+30 09 36	0.2078	11	Low SNR(c)
SLJ1204.4–0351	12304	12 04 22.9	–03 50 55	0.2609	23	Standard
SLJ1335.7+3731	12307	13 35 45.6	+37 31 48	0.4070	27	Standard
SLJ1337.7+3800	12306	13 37 43.7	+38 00 57	0.1798	34	Low SNR(a)
SLJ1602.8+4335	12308	16 02 52.8	+43 35 24	0.4155	42	Standard
SLJ1634.1+5639	12309,13145	16 34 12.0	+56 39 36	0.2377	48	Low SNR(a)

in the 0.7 – 2.0 keV band) into a projected emissivity profile, which is modeled by projecting a density model along the line of sight. We use the model of Vikhlinin et al. (2006, see that work for parameter definitions):

$$n_{\rm p}n_{\rm e} = \frac{n_0^2(r/r_c)^{-\alpha}}{(1+r^2/r_c^2)^{3\beta-\alpha/2}} \times (1+r^\gamma/r_s^\gamma)^{-\epsilon/\gamma} \quad (1)$$

The same parameter constraints were employed as in Vikhlinin et al. (2006) i.e. γ is fixed at 3 and ϵ <5 to exclude nonphysical sharp density peaks. Gas masses were determined from Monte Carlo realisations of the projected emissivity profile based on the best fitting projected model to the original data.

The cluster temperature, gas mass and r_{500} (the radius at which the enclosed density of the cluster becomes 500 times the critical density at the cluster's redshift) were determined through an iterative process. We extract a spectrum from within an estimate of r_{500} (with the central 15% excluded), integrate a gas density profile (see Maughan et al. 2008) to determine the gas mass, and then calculate a value for $Y_{\rm X}$ (the product of the temperature and gas mass; Kravtsov, Vikhlinin & Nagai 2006). A new r_{500} was then estimated from the $Y_{\rm X}$–M scaling relation of Vikhlinin et al. (2009a),

$$M_{500} = E(z)^{-2/5} A_{\rm YM} \left(\frac{Y_{\rm X}}{3\times10^{14} M_\odot {\rm keV}} \right)^{B_{\rm YM}} \quad (2)$$

with $A_{\rm YM} = 5.77\times10^{14}{\rm h}^{1/2}{\rm M}_\odot$ and $B_{\rm YM} = 0.57$. Here, M_{500} is the mass within r_{500}, where r_{500} is defined as $r_{500} = (3M_{500}/4\pi500\rho_{\rm c}({\rm z}))^{1/3}$, where $\rho_{\rm c}$(z) is the critical density of the universe at the cluster redshift. The $Y_{\rm X}$–M_{500} relation assumes self-similar evolution (corrected by $E(z)^{-2/5}$), where $\mathrm{E(z)} = \sqrt{\Omega_{\rm M}(1+z)^3 + (1-\Omega_{\rm M}-\Omega_\Lambda)(1+z)^2 + \Omega_\Lambda}$ (justified by Maughan 2007). An initial temperature of 2 keV was used to determine an initial r_{500} and then this process was repeated until r_{500} converged to within 1%. The luminosity and temperature were measured from spectra extracted within $\rm r_{500}$ both with and without the central 15% of r_{500} excluded. Throughout we define $L_{\rm X}$ and kT as core excluded cluster properties, and $L_{\rm X,c}$ and $kT_{\rm c}$ as core included properties. All luminosities quoted throughout are bolometric unless otherwise stated.

3.2 The "Low SNR" Method

Due to the low SNR of the clusters resulting from the clusters being less luminous than expected based on the WL mass (used when planning the observations), five of the clusters in our sample could not be analysed using the method described in Sect. 3.1. We therefore used a variety of methods in order to obtain the most accurate properties for these low SNR clusters. In order of preference, these were:

(a) When the gas mass could not be reliably measured, we used the temperature alone to measure r_{500}. We used the r_{500}-T relation given in Vikhlinin et al. (2006), and followed the iterative process detained in Sect. 3.1 to determine the cluster properties within r_{500}. We note that for consistency with the r_{500}-T relation, the central 70 kpc is excluded (instead of 0.15%r_{500} as in § 3.1).

(b) Extracting a spectrum within the highest SNR region for the cluster and determining the properties within this region. $\rm r_{500}$ was then estimated using the r_{500}-T of Vikhlinin et al. (2006) and Lx was extrapolated to the radius by integrating under a β-profile with r_c=150 kpc and β=0.667. Again, the central 70 kpc is excluded for this analysis.

(c) Using PIMMS[4] to determine the cluster luminosity from the count rate of the cluster observation when no spectroscopic analysis could be performed. A global temperature of 2 keV was assumed for the cluster, and the count rate determined in an r_{500} determined from the r_{500}-T relation of Vikhlinin et al. (2006).

3.3 Notes on Individual Clusters

Notes on the WL detections of the individual clusters can be found in Hamana et al. (2009). In this section we note any peculiarities or points of interest for observations in which we departed from analysis process described in Sect. 3.1. We note that five of the observations in our cluster sample were analysed using the method described in Sect. 3.2, and these clusters are discussed below.

[4] http://cxc.harvard.edu/toolkit/pimms.jsp

3.3.1 SLJ0225.7–0312

The cluster SLJ0225.7–0312 had an archival *XMM* observation taken in the XMM_LSS_13 field. An image of the *XMM* observation is shown in Figure A1(a). The properties of the cluster were obtained following method (b) outlined in Sect. 3.2. A spectrum was extracted within [0-433]kpc for each of the *XMM* cameras and the spectra fit simultaneously with the temperature of the hot APEC components tied together. The net counts in the 0.3–7.0 keV band were 2635, 1019 and 1053 for the pn, mos1 (m1) and mos2 (m2) cameras respectively, with SNR 40, 24 and 25 for the pn, m1 and m2 cameras respectively. Due to the large field of view of the *XMM* cameras, a local background region was used for background subtraction. We found a temperature of kT=2.93±0.19 keV for the cluster, corresponding to an r_{500} of 798 kpc. We found an extrapolated luminosity within r_{500} for the cluster of $L_{\rm X}$=(7.31±0.19)×10^{43} ergs s^{-1}. The analysis carried out above was also employed to determine the properties of the cluster with the core included. We derived a temperature of $kT_{\rm c}=3.00^{+0.18}_{-0.17}$ keV. Extrapolating outwards to r_{500}, we determined a luminosity of $L_{\rm X,c}$=(7.90±0.19)×10^{43} ergs s^{-1}.

3.3.2 SLJ1000.7+0137

The cluster SLJ1000.7+0137 had three archival *Chandra* observations taken in the COSMOS-6 field. An image of the *Chandra* observation is shown in Figure A3(a). The three individual observations were analysed separately as described in Sect 3.1. The data were then combined for certain stages of the analysis. Source, background and exposure maps were projected onto common coordinated systems and summed. Source and background spectra were extracted for individual observations and fit simultaneously with the temperatures of the hot APEC components tied together.

3.3.3 SLJ1135.6+3009

In order to calculate the luminosity of this cluster, we followed method (c) outlined in Sect. 3.2. We determined the number of counts in a region centered on the location of the Brightest Central Galaxy (BCG, see Figure A4 with the BCG highlighted by the black circle), subtracting the number of counts from the same region in a blank-sky background obtained for the observation, scaled by the ratio of the source and background exposure times. The net number of counts obtained was 71±22 (significant at the 3.2σ level), in the 0.7–2.0 keV band. We calculated a bolometric luminosity of $L_{\rm X,c}$=(1.28±0.40)×10^{43} ergs s^{-1} for the cluster, with the errors derived assuming Poisson statistics.

3.3.4 SLJ1337.7+3800

To determine the cluster properties we used method (b) in Sect. 3.2, extracting spectra within a radius [70-215]kpc. The net number of spectral counts, corrected for background, was then 130 (in the 0.6–9.0 keV band, with SNR=5.3). We find a temperature of $kT=1.63^{+0.68}_{-0.28}$ keV, corresponding to an r_{500} of 574 kpc. We derive an extrapolated bolometric luminosity of the cluster of $L_{\rm X}$=(6.58±1.31)×10^{42} ergs s^{-1}. This analysis was repeated including the core (obtaining 172 net spectral counts in the 0.6–9.0 keV band, with SNR=6.45). We determined a temperature of $kT_{\rm c}=1.63^{+0.47}_{-0.23}$ keV and an extrapolated bolometric luminosity of $L_{\rm X,c}$=(8.56±1.21)×10^{42} ergs s^{-1}.

3.3.5 SLJ1634.1+5639

Due to observational constraints, the exposure was split into two observations. Therefore the analysis of the cluster was performed as described in Sect. 3.3.2. The properties of this cluster were obtained following the process outlined in method (a) in Sect. 3.2. We find a temperature of $kT=1.37^{+0.80}_{-0.44}$ keV and $L_{\rm X}$=(4.17±1.67)×10^{42} ergs s^{-1}. Including the core of the cluster we found a temperature and luminosity of $kT_{\rm c}=1.72^{+0.95}_{-0.43}$ keV and $L_{\rm X,c}$=(6.78±2.59)×10^{42} ergs s^{-1}.

Substructure in SLJ1634 appears likely on the basis of the locations of the galaxies, as marked in Figure A9, which shows a split in the population of galaxies in the northern and southern region of the cluster. To check for the reality (or otherwise) of this structure, a tree analysis of the locations of the galaxies in 3D (position, velocity, redshift) space was undertaken. The results suggest a composite structure for the cluster, with the galaxies separated into three separate groups. The galaxies in Figure A9 are colour coded with respect to each group they are associated. Group A (magenta squares), B (black squares) and C (green squares) have a redshift of 0.231, 0.238 and 0.242 respectively. This composite structure may explain the large offset in the luminosity-mass relation for SLJ1634 when the WL mass is calculated centered on the X-ray peak (see Figs 5,6).

3.3.6 SLJ1647.7+3455

Although a dedicated *Chandra* observation was obtained for the cluster SLJ1647.7+3455, due to the non-detection of the cluster, no useful information could be determined. We therefore used an archival *XMM* observation to determine the properties of the cluster, following the method outlined in Sect 3.2(a). The spectra were analysed in the same way as in Sect 3.3.1. We obtained a temperature of $kT=1.49^{+0.11}_{-0.11}$ keV and $L_{\rm X}$=(1.38±0.12)×10^{42} ergs s^{-1}. Including the cluster core, we find $kT_{\rm c}=1.58^{+0.09}_{-0.10}$ keV and $L_{\rm X,c}$=(1.57±0.12)×10^{42} ergs s^{-1}.

4 RESULTS

In this section we present the results of our analysis of our 10 WL selected clusters. We derive various scaling relations for these clusters and compare to published results. The measured properties of the clusters are given in Table 2, along with the WL mass determined in Hamana et al. (2009) converted to H_0=70 km s^{-1} Mpc^{-1}. We note two updates to the derivation of the WL masses given in Hamana et al. (2009), and those presented in this work. We use the halo mass-concentration relation of Duffy et al. (2008), and the modified NFW profile given in Oguri & Hamana (2011)

Table 2. Derived X-ray properties of the clusters with WL mass estimates (see § 4). Clusters in the top part of the table were analysed from *XMM* observations, in the bottom part from *Chandra* observations.

Cluster	E(z)	$L_{\rm X}$ ($\times10^{43}$ ergs s^{-1})	$L_{\rm X,c}$ ($\times10^{43}$ ergs s^{-1})	$L_{0.1-2.4{\rm keV,X,c}}$ ($\times10^{43}$ ergs s^{-1})	kT keV	$kT_{\rm c}$ keV	$M_{\rm WL,500}$ ($\times10^{14}{\rm M}_{\odot}$)
SLJ0225.7–0312	1.070	7.31±0.19	7.90±0.19	4.16±0.10	$2.93^{+0.19}_{-0.19}$	$3.00^{+0.18}_{-0.17}$	$1.97^{+0.47}_{-0.47}$
SLJ1647.7+3455	1.140	1.38±0.12	1.57±0.12	1.31±0.09	$1.49^{+0.11}_{-0.11}$	$1.58^{+0.09}_{-0.10}$	$2.00^{+0.67}_{-0.79}$
SLJ0850.5+4512	1.100	0.78±0.14	0.92±0.13	0.83±0.13	$1.21^{+0.22}_{-0.16}$	$1.16^{+0.14}_{-0.15}$	$1.09^{+0.39}_{-0.43}$
SLJ1000.7+0137	1.114	4.04±0.17	5.62±0.19	3.80±0.17	$2.43^{+0.29}_{-0.29}$	$2.61^{+0.41}_{-0.23}$	$2.39^{+0.46}_{-0.53}$
SLJ1135.6+3009	1.108	–	1.28±0.40	1.08±0.26	–	–	$2.49^{+0.50}_{-0.56}$
SLJ1204.4–0351	1.141	3.43±0.35	3.97±0.38	2.92±0.28	$2.16^{+0.49}_{-0.37}$	$2.16^{+0.59}_{-0.22}$	$1.20^{+0.50}_{-0.60}$
SLJ1335.7+3731	1.239	3.10±0.71	3.99±0.69	3.35±0.68	$1.39^{+0.63}_{-0.37}$	$1.78^{+0.79}_{-0.47}$	$2.79^{+0.90}_{-1.01}$
SLJ1337.7+3800	1.092	0.66±0.13	0.86±0.12	0.37±0.05	$1.63^{+0.68}_{-0.28}$	$1.63^{+0.47}_{-0.23}$	$1.24^{+0.36}_{-0.39}$
SLJ1602.8+4335	1.245	12.7±1.14	16.4±1.22	8.50±0.54	$3.91^{+1.72}_{-0.88}$	$4.45^{+1.29}_{-1.12}$	$2.66^{+0.69}_{-0.71}$
SLJ1634.1+5639	1.126	0.63±0.22	0.68±0.26	0.49±0.15	$1.37^{+0.77}_{-0.23}$	$1.42^{+0.83}_{-0.23}$	$0.87^{+0.39}_{-0.49}$

4.1 The Luminosity-Temperature Relation

Here we derive the X-ray luminosity-temperature relation for our clusters, omitting SLJ1135 for which a temperature could not be obtained. Figure 1 shows the $L_{\rm X,c}$-$kT_{\rm c}$ relation for our clusters (red triangles) compared with the LT relation given in Maughan et al. (2012, blue open circles). The Maughan et al. (2012) sample of clusters was selected from all available *Chandra* pointings as of 2006 November, correlated with the NASA/IPAC Extragalctic Database (NED) and observations with a galaxy group or cluster listed in NED within 10′ of the *Chandra* aimpoint were kept. Further criteria included observations only carried out with the ACIS-I detector, a galaxy group/cluster as the target, and a published redshift >0.1. As the Maughan et al. (2012) sample of clusters covers a wide redshift range ($0.1<z<1.3$), the luminosities of the clusters were corrected for the expected self-similar evolution, given by $L_{\rm X}\times{\rm E(z)}^{-1}$. The same correction was also applied to our data.

A power law of the form $L_X = E(z)^2 L_0 (kT/kT_0)^{B_{LT}}$ was fit to the data using the BCES orthogonal regression in log space (Akritas & Bershady 1996) with kT_0 set at 2 keV. From our fit we find a normalisation of $L_0=(2.44\pm0.51)\times10^{43}$ ergs s^{-1} and a slope of $B_{\rm LT}=2.63\pm0.69$. The slope and normalisation are consistent with the fit to the Maughan et al. (2012) sample, who find a normalisation of $L_{0,\rm M12}=(2.40\pm0.78)\times10^{43}$ ergs s^{-1} at 2 keV and a slope of $B_{\rm LT,M12}=3.63\pm0.27$ (see Fig 1, blue solid line). We conclude that the X-ray properties of the WL selected clusters scale consistently with X-ray selected clusters in the luminosity-temperature plane.

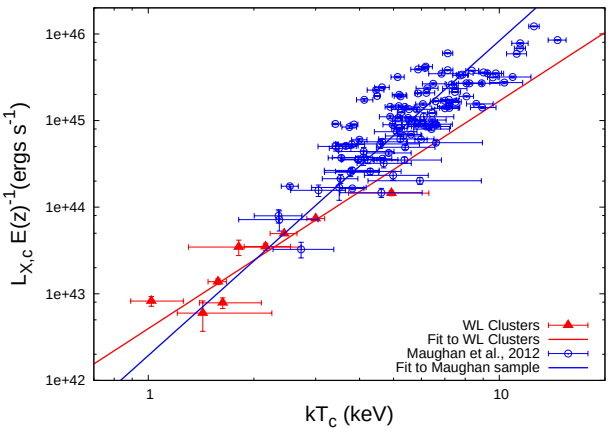

Figure 1. Figure showing the core included luminosity-temperature ($L_{\rm X,c}$-$kT_{\rm c}$) relation for the WL selected clusters (red circles). For comparison we over-plot the $L_{\rm X,c}$-$kT_{\rm c}$ relation of a sample of 114 X-ray selected clusters of Maughan et al. (2012, blue open circles).

4.2 The Luminosity-Mass Relation

Here we derive the luminosity-mass (LM) relation for our clusters, with the masses estimated from the WL analysis presented in Hamana et al. (2009), updated as described in Section 4. Figure 2 shows the luminosity-mass relation for our clusters (red triangles), and compared to the data given in Mantz et al. (2010a, black crosses). Their clusters are taken from the ROSAT Brightest Clusters Sample (BCS; Ebeling et al. 1998), the *ROSAT*-ESO Flux-Limited X-ray Sample (REFLEX; Böhringer et al. 2004), and the bright sub-sample of the Massive Cluster Survey (Bright MACS; Ebeling et al. 2010), all $z<0.5$. We note that Mantz et al. (2010a) uses the gas mass as a robust, low-scatter proxy for the total cluster mass. The luminosities in Mantz et al. (2010a) are calculated in the 0.1–2.4keV band (cluster rest frame), we therefore calculate the luminosities of the WL clusters in this band for the purpose of this comparison.

Since we wish to compare weak-lensing and X-ray selected clusters, we need to minimise any selection effects in the X-ray comparison sample. X-ray selected cluster samples suffer from both Malmquist and Eddington biases. Malmquist bias refers to the effect that a larger survey volume finds more luminous objects for a given flux limit, and Eddington bias refers to the differential scattering of objects across the detection threshold of a survey due to the slope of the mass function. The analysis presented in Mantz et al. (2010a) takes fully into account these biases, making it an ideal comparison for this work. We also note that the correction for the E(z) factor in Mantz et al. (2010a) for the LM relation was based upon the best fit cosmology found in

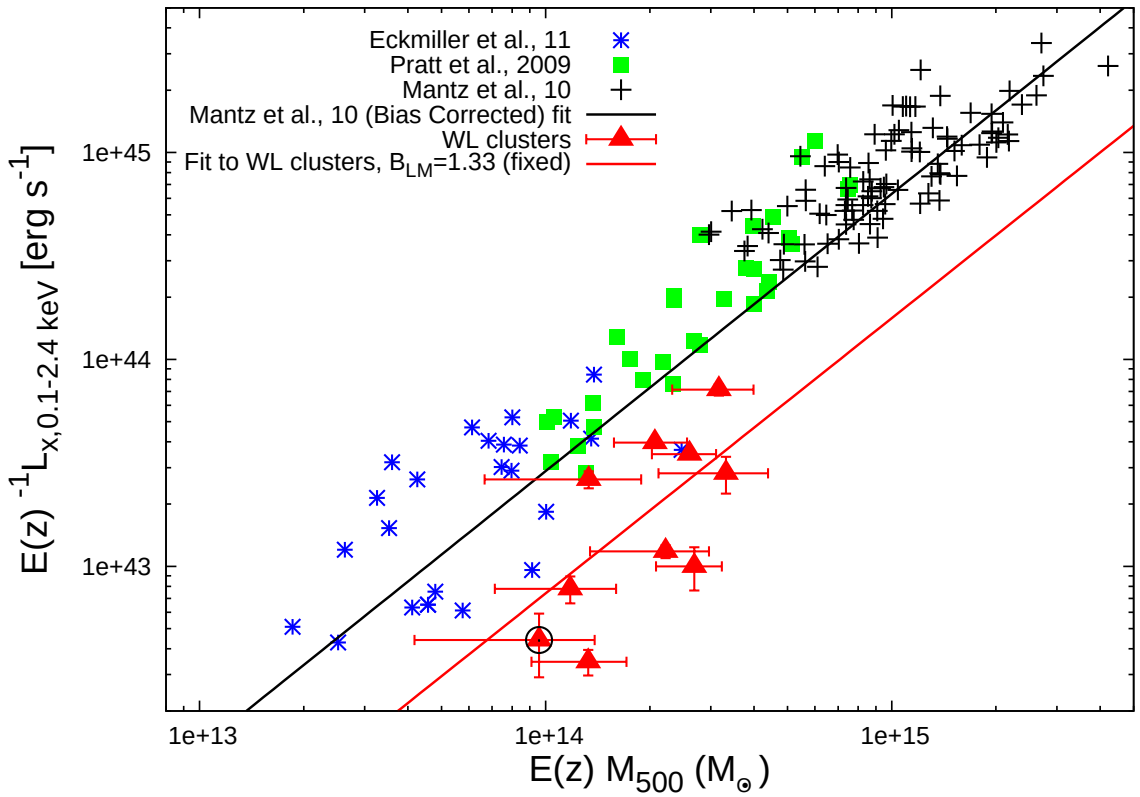

Figure 2. The luminosity-mass (LM) relation for our WL selected clusters (red triangles), whose masses are derived from WL. The cluster SLJ1634 is highlighted by the black circle. For comparison we plot the data of X-ray selected clusters given in Mantz et al. (2010b, black crosses), and the corresponding fit taking into account selection effects (black line). Further comparisons are made to the REXCESS cluster sample (Pratt et al. 2009, green squares) and galaxy group sample of Eckmiller, Hudson & Reiprich (2011, blue stars)

Mantz et al. (2010b). For the purposes of the LM relation comparison, the E(z) factor for each cluster is also calculated using the Mantz et al. (2010b) cosmology. On average, $E(z)$ changes by ≈3%.

A power law of the form $E(z)^{-1}L_{\rm X} = L_0(E(z)M/M_0)^{B_{\rm LM}}$ was fit to the WL clusters in log space, with M_0 set at $2\times10^{14}{\rm M}_\odot$. Due to the low quality of the data and the small number of data points we fixed the slope ($B_{\rm LM}$) of the relation at the self similar expectation of 1.33. We note that since the slope is fixed, we perform a χ^2 fit to the cluster LM relation. For a mass of $2\times10^{14}{\rm M}_\odot$ we found $L_0=(1.9\pm0.2)\times10^{43}$ ergs s^{-1} (see red solid line Figure 2). The fit from Mantz et al. (2010b) is represented by the solid black line. The low normalisation compared to the data demonstrates the size of the Malmquist and Eddington biases (which were included in the analysis of the Mantz et al. (2010b) data. The Mantz et al. (2010b) LM relation at the same mass predicts L_0=7.3×10^{43} ergs s^{-1}. Compared with X-ray selected clusters, X-ray luminosity is lower at a given mass by a factor 3.9±0.9. Conversely, $M_{\rm WL,500}$ is higher for a given luminosity by a factor 2.9±0.2. We discuss the nature of this large offset in the LM relation in Sect. 5.

The main drawback in the comparison with the Mantz et al. (2010b) sample of clusters is the mass range covered by the respective cluster samples. The Mantz et al. (2010b) sample of clusters have masses M_{500} ≥2.7×10^{14}M$_\odot$, whereas our WL sample are all <2.7×10^{14}M$_\odot$. To ensure the mass range of the comparison sample is not playing a role in the large observed offset, we compare to a sample of clusters probing the lower mass end and a sample of galaxy groups. We use the REXCESS (Böhringer et al. 2007) sample of clusters studied in Pratt et al. (2009) which span the mass range ≈10^{14}-10^{15}M$_\odot$, and the sample of galaxy groups presented in Eckmiller, Hudson & Reiprich (2011) spanning the mass range ≈0.05-2×10^{14}M$_\odot$. The masses of the Pratt et al. (2009) clusters were calculated using the $Y_{\rm X}$-Mass relation given in Arnaud, Pointecouteau & Pratt (2007), and the masses of the Eckmiller, Hudson & Reiprich (2011) groups were calculated by assuming hydrostatic equilibrium and spherical symmetry (see Sect. 3.4 in Eckmiller, Hudson & Reiprich 2011). In both cases the luminosities are calculated in the 0.1-2.4 keV band (cluster rest frame). We plot the clusters on the LM relation in Figure 2, with the Pratt et al. (2009) clusters given by the green squares and the Eckmiller, Hudson & Reiprich (2011) groups given by the blue stars. A visual inspection shows that all the X-ray selected comparison groups lie on approximately the same LM relation. Although the Pratt et al. (2009) and Eckmiller, Hudson & Reiprich (2011) samples appear to lie slightly above the Mantz et al. (2010b) relation, this is consistent with a similar amount of bias as in the Mantz et al. (2010b) sample, with the relation correcting for these effects. The offset of

the WL selected clusters is still evident down to these low masses.

4.3 X-ray Morphology of Weak Lensing Selected Clusters

4.3.1 The dynamical state of weak lensing selected clusters

We wish to investigate the dynamical state of our WL selected clusters as compared to X-ray selected cluster samples. We use the centroid shift method of Poole et al. (2006) to determine the dynamical state of the cluster. The centroid shift ($\langle w \rangle$) was defined as the standard deviation of the distance between the X-ray peak and centroid, measured within a series of circular apertures centered on the X-ray peak and decreasing in steps of 5% from r_{500} to $0.05r_{500}$. The $\langle w \rangle$ values are given in Table 3. Maughan et al. (2012) used $\langle w \rangle$ to distinguish between "relaxed" and "unrelaxed" clusters. For the Maughan et al. (2012) sample of 114 clusters they adopted a value of $\langle w \rangle$=$0.006r_{500}$ below which clusters are classed as "relaxed", and above which are classed as "unrelaxed". Using this threshold value, 25% of the Maughan et al. (2012) sample was classed as "relaxed". If we adopt this value for our sample of WL selected clusters, we find that none of the clusters in Table 3 qualify as "relaxed".

The value of $\langle w \rangle$ is somewhat subjective, and the value used to separate relaxed and unrelaxed clusters can depend on the sample of clusters used, and indeed on each individual study. Pratt et al. (2009) used the REXCESS sample of clusters and defined relaxed/unrelaxed clusters using the same method of calculating $\langle w \rangle$ as we employ here. Pratt et al. (2009) found that ∼60% of their clusters has $\langle w \rangle$ <0.01, while for our WL clusters we find that only one of the seven clusters with measurable $\langle$w$\rangle$ values are below this threshold. We note however that this comparison is only based on a small number of clusters from the WL.

This result appears analogous to the recent cluster sample from the early release Planck all sky survey (Planck Collaboration et al. 2011b). These clusters were detected via their SZ signals, and 25 candidates were followed up with snapshot *XMM* observations. Through a visual inspection of the gas density profiles constructed for each cluster, a large proportion of these SZ selected clusters appear morphologically disturbed. Since the WL selected clusters studied in our sample also appear to be morphologically disturbed, selecting clusters from either their SZ or WL signal, as compared to selecting cluster via their X-ray emission, appears to give a more representative distribution of morphologies for clusters.

4.3.2 The cool-core fraction of weak lensing selected clusters

The absence of relaxed clusters in our sample as indicated by $\langle w \rangle$ suggests we should also see few cool core (CC) clusters. This also has important implications for cosmology as the CC fraction and its evolution may be over-represented/biased in X-ray samples (Santos et al. 2010). This result is not unexpected due to the high X-ray surface brightness at the center of CC clusters, making them easier to detect in X-ray cluster surveys. Hudson et al. (2010) presented a comprehensive study of 16 CC diagnostics for the HIFLUGCS sample of 64 clusters. They found that, for clusters with low data quality, the cuspiness of the gas density profile is the preferred method of determine the presence of a CC. Cuspiness is defined as the logarithmic slope of the gas density profile at a radius of $0.04r_{500}$, modeled using the gas density profiles given by equation 1, with the uncertainties derived from the cuspiness values measured from Monte Carlo realisations of the gas density profile. We obtained the cuspiness values from gas density profiles fitted to surface brightness profiles derived from images binned by a factor 2, with each radial bin containing at least 10 cluster counts. The same fitting process was followed as in § 3.1 and the cuspiness values were derived from these profiles. Table 3 lists the values of the cuspiness for each cluster where a gas density profile could be obtained.

Table 3. Table of the derived dynamical properties of the cluster sample.

Cluster	$\langle w \rangle (10^{-3} r_{500})$	cuspiness	$\epsilon_{\rm bcg}$
SLJ0225.7–0312	–	–	0.07
SLJ1647.7+3455	–	–	0.15±0.01
SLJ0850.5+4512	31±28	$0.71^{+0.44}_{-0.64}$	0.13±0.01
SLJ1000.7+0137	105±4	$0.02^{+0.15}_{-0.01}$	0.20±0.02
SLJ1135.6+3009	–	–	0.40±0.01
SLJ1204.4–0351	28±13	$0.13^{+0.55}_{-0.08}$	0.16±0.02
SLJ1335.7+3731	12±8	$0.24^{+0.48}_{-0.17}$	0.11±0.02
SLJ1337.7+3800	44±30	$0.97^{+0.19}_{-0.16}$	0.23±0.01
SLJ1602.8+4335	7±4	$0.53^{+0.17}_{-0.51}$	0.14±0.02
SLJ1634.1+5639	87±85	–	0.15±0.01

Maughan et al. (2012) also used the cuspiness to determine the presence of a CC in their sample of 114 clusters. Above a value of 0.8 clusters were considered to host a CC, and below they were not. If we adopt this value for our sample of 6 clusters with measurable cuspiness, we find that one of the clusters is considered to host a CC. We note that the Maughan et al. (2012) sample spans a wide range in redshift and data quality, and again the threshold in cuspiness used to define CC/NCC clusters is subjective depending on the sample being studied. The Hudson et al. (2010) sample consists of clusters with very high data quality and the value of the cuspiness is well constrained for all clusters. Hudson et al. (2010) adopted a value for cuspiness of 0.7 to segregate between CC and non-CC clusters. If we adopt this value of cuspiness for our sample of clusters, we find only 2/6 of the clusters host a CC. In both cases we find a smaller percentage of CC clusters in comparison to these samples of clusters, we find 16.6% of clusters host a CC when using a cuspiness value of 0.8, as compared to 26.3% found in Maughan et al. (2012). We find that 33.3% of clusters host a CC when using a cuspiness value of 0.7, as compared to 54.7% found in Hudson et al. (2010). This suggests that CC clusters may be over-represented in X-ray selected samples of clusters.

5 DISCUSSION

In Sect. 4.2 we showed that WL selected galaxy clusters are underluminous by a factor ≈3.9 for a given mass, compared to X-ray selected clusters. In terms of the mass, we find

that the WL selected clusters are over-massive by a factor ≈3 compared to X-ray selected clusters. The consistency of the $L_{\rm Xc}$-$kT_{\rm c}$ relation with X-ray selected clusters (see Fig 1) suggests that the discrepancy may more likely arise as a result of a bias in the mass. We therefore first investigate the nature of this offset through a study of systematic effects on the WL mass estimates.

5.1 Possible Systematics in the WL Masses

In the following sections we present a series of plausible effects that could bias the WL mass. These biases are presented as a cumulative effect on the WL mass, and we investigate the effect these biases have on the LM relation.

5.1.1 The Effect of Cluster Centre Position on Weak Lensing Mass

The X-ray analysis presented in this paper is independent of the WL analysis given in Hamana et al. (2009), and as such, different locations of the cluster centre are used for the two analysis. The WL masses given in Table 2 are derived from fitting NFW models to shear profiles centered on the peak position in the WL mass maps, whereas the luminosities are derived centered on the X-ray centriod. Here we investigate the effect of deriving the WL masses from profiles centered on the X-ray centroid.

Figure 3 shows the ratio of the WL mass centered on the peak of the WL signal to the WL mass centered on the X-ray centroid ($M_{500}^{\rm WLpeak}/M_{500}^{\rm Xcent}$) against the offset of the WL peak and X-ray centroid (in units of r_{500}). The cluster SLJ1634 is highlighted by the black circle. This cluster shows evidence for a composite structure (see §3.3.5) and the WL mass decreases by a factor ∼7 when centered at the X-ray peak. We note for the cluster SLJ1135, the X-ray analysis was centered on the WL peak due to the low SNR of the X-ray data, and no X-ray centroid could be obtained. It is thought that any offset between the WL and X-ray would be minimal since the WL peak is aligned closely with the BCG of the cluster (see Fig A4(b)). This figure shows that the ratio of the masses is consistent with a ratio of 1.0 (given by the black dashed line). This result is unsurprising due to the radial range within which the WL masses are derived ($2<\theta<20'$), to neglect contamination from cluster galaxies. These results are consistent with the results from Okabe et al. (2010a), who find that the relative inaccuracy of cluster centroid position has a negligible effect on the resulting χ^2 value of the NFW fit to their distortion profiles, and hence the mass derivation.

The effect of using WL masses centered on the X-ray centroid on the LM relation is shown in Figure 5(dashed blue line). The original LM relation from Figure 2 is given by the dashed green line. By calculating the WL masses centered on the X-ray centroids, the masses have decreased on average by a factor of ≈1.1.

5.1.2 "Deboosting" the Weak Lensing Mass Estimates

Here we correct the weak lensing masses by "deboosting" the shear signal, which is analogous to the effect of Eddington bias (see Sect 4.2). Since our sample is based upon a noisy

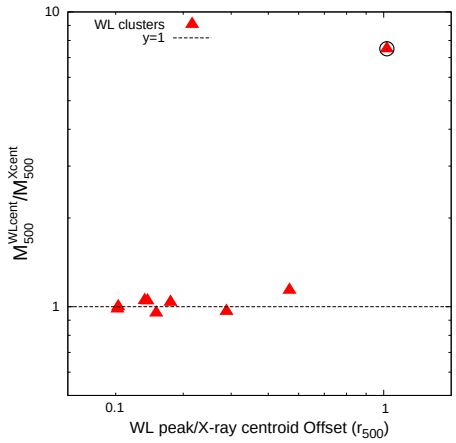

Figure 3. Plots the ratio of the WL mass derived within the X-ray r_{500} at the WL peak and X-ray centroid, against the offset of the WL peak and X-ray centroid (plotted in units of r_{500}). The cluster SLJ1634 is highlighted by the black circle.

indicator of the cluster mass, the shear signal (κ), clusters with high mass but a low observed κ will not be included in our sample, and conversely clusters with low masses but high observed shear will be included in our sample. Our cluster sample will therefore be biased to clusters with a high shear signal relative to their mass, and due to the slope of the mass function, there will be more low mass than high mass clusters close to our detection limit. The overall effect will be to measure high mass values, due to the high shear signal, and so bias the sample to higher masses. An application of "deboosting" can be found in Coppin et al. (2006) for a SCUBA source catalog.

In order to calculate "deboosted" mass estimates, we follow a similar method to that carried out in Coppin et al. (2006). Initially, the cluster mass is estimated from the shear profile (κ) via χ^2 fitting with an NFW model. We also have a theoretical prediction of the shear profile for a modified NFW profile. We compute the χ^2 following the standard procedure from the observed shear profile and the model prediction as a function of halo mass M (χ^M). From χ^M we compute the best-fit (non-"deboosted") WL mass and likelihood interval. Next we consider $P = \exp(-\chi^2/2)$ as $P(\kappa, \sigma \mid M)$, and consider the halo mass function as p(M). From Bayes' theorem we therefore have $P(M \mid \kappa, \sigma) = P(M)P(\kappa, \sigma \mid M)$. We then compute $\chi^2_{\rm deboost} = -2\ln(P(M \mid \kappa, \sigma))$ and find the best fit mass and the likelihood function.

This correction decreases the WL mass by an average of ≈1.27. This is shown in Figure 5 as the dotted pink line, representing the cumulative effect of the centroid position (see § 5.1.1) and Eddington bias on the LM relation.

5.1.3 Weak Lensing Biases due to Halos Elongated Along the Line of Sight

An additional bias involved in the estimation of weak lensing masses is that due to a triaxial shape of the cold dark matter (CDM) halo (Warren et al. 1992; Jing & Suto 2002; Shaw et al. 2006). This can lead to errors in the weak lensing masses by ±(10-50)% when spherical symmetry is assumed

(Corless & King 2007; Meneghetti et al. 2010; Becker & Kravtsov 2011; Bahé, McCarthy & King 2012). In order to correct for the effect of a triaxial CDM halo we use the set of simulated clusters studied in Meneghetti et al. (2010). Figure 17 of Meneghetti et al. (2010) shows the ratio of the weak+strong lensing mass (a nonparametric method combining both strong and weak lensing regimes to calculate cluster mass) to true cluster mass as a function of angle with the projection axis (the angle between the major axis of the cluster inertia ellipsoid and the axis along which the mass distribution is projected). Since our weak lensing masses are based upon NFW profiles, we combine Figure 17 with Figure 16(a) from Meneghetti et al. (2010), to derive the same relation appropriate for NFW profile mass estimates.

It is noted in Marrone et al. (2012) that their plot of fractional deviation in mass from a self-similar $M_{500,\mathrm{WL}}$-Y_{sph} as a function of brightest cluster galaxy (BCG) ellipticity (ϵ_{BCG}) looks strikingly similar to Figure 17 presented in Meneghetti et al. (2010). They find that clusters with a BCG ellipticity $\leq$0.15 have the largest deviation in mass from the self-similar relation. By considering BCGs as prolate systems whose major axis is aligned with the major axis of the CDM halo, circular BCGs indicate the major axis is close to the line of sight (LOS) through the cluster. The viewing angle (ψ) can be calculated as a function of the observed axis ratio (q) and intrinsic BCG axis ratio (δ), using

$$\psi = \arccos\left(\sqrt{\frac{1-(\delta/q)^2}{1-\beta^2}}\right) \qquad (3)$$

where $q = b/a$, and adopting $\delta = 0.67$ (Fasano et al. 2010). A ϵ_{BCG}=0.15 corresponds to a viewing angle of $\psi \simeq 34°$, we therefore use clusters below this angle from Meneghetti et al. (2010) to calculate the average of the weak lensing mass to true mass and correct our masses by this factor.

In order to correct our weak lensing masses, we calculate ϵ_{BCG} for each cluster from the *Subaru* images. For clusters which have ϵ_{BCG} $\leq$0.15 (i.e. with a viewing angle $\leq$34°), we divide the corresponding WL mass by 1.17, and clusters with ϵ_{BCG} >0.15 have their masses divided by 0.93. The LM relation corrected for triaxiality, Eddington bias and centroid position is given by the dashed-dotted cyan line in Figure 5.

By calculating ϵ_{BCG} for each of our clusters, we have found that 60% appear to be viewed near the LOS, suggesting that weak lensing surveys preferentially select clusters elongated along the LOS. Comparing to Marrone et al. (2012), an X-ray selected cluster sample, only ∼18% of their clusters have ϵ_{BCG} $\leq$0.15.

5.1.4 Weak Lensing Masses within X-ray r_{500}

As stated in § 5.1.1, the original WL analysis was independent of the X-ray analysis. The LM relation shown in Figure 2 had the masses derived within a WL derived r_{500} (r^{WL}_{500}) and the luminosities calculated within an X-ray derived r_{500} (r^{X}_{500}). In order to compare consistently with the Mantz et al. (2010b) LM relation, whose masses were derived within r^{X}_{500}, we recalculate the WL masses within r^{X}_{500} for each cluster. Figure 4 plots the change in WL mass against the ratio of the WL and X-ray derived r_{500}. The WL masses decrease on average by a factor of ≈1.6. The correction for centroid position, Eddington bias, triaxiality and the calculation of the WL mass within r^{X}_{500}, is given by the red solid line in Figure 5.

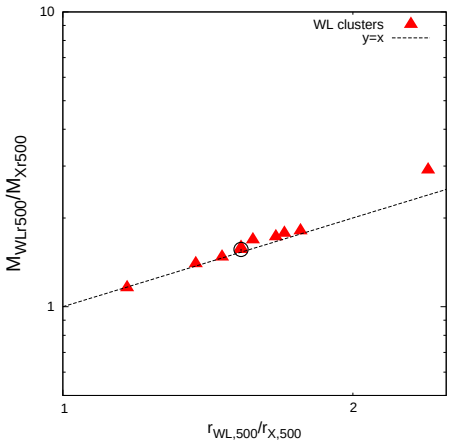

Figure 4. Plots the ratio of the WL mass derived within the WL $r_{WL,500}$ and X-ray $r_{X,500}$, against the ratio of $r_{WL,500}/r_{X,500}$. The cluster SLJ1634 is highlighted by the black circle.

Table 4. Table of corrections applied to the WL derived mass for each cluster.

	Correction			
Cluster	Centroid	Edd. Bias	Ellipticity	r_{500}
SLJ0225.7–0312	1.05	1.20	1.17	1.16
SLJ1647.7+3455	0.93	1.34	1.17	1.73
SLJ0850.5+4512	1.10	1.34	1.17	1.80
SLJ1000.7+0137	1.26	1.12	0.93	1.68
SLJ1135.6+3009	1.28	1.12	0.93	1.78
SLJ1204.4–0351	0.94	1.54	0.93	1.40
SLJ1335.7+3731	1.10	1.34	1.17	2.92
SLJ1337.7+3800	–	1.28	0.93	1.48
SLJ1602.8+4335	0.98	1.18	1.17	1.59
SLJ1634.1+5639	–	–	–	–

From Figure 5 we can clearly see the largest correction to the WL masses is when they are determined within X-ray derived r_{500} values. However, this partially obscures the true discrepancy. This shows that the agreement between WL and X-ray masses is improved if the same aperture is used for both, but this is no longer a WL M_{500}. We investigate this further in Section 5.3.

5.1.5 Corrected Luminosity-Mass Relation

In Sections 5.1.1, 5.1.2, 5.1.3 and 5.1.4, we presented a series of systematic and statistical corrections to our WL cluster masses. We re-derive the LM relation for the WL selected clusters, with the WL masses corrected for these effects. Figure 5 plots the corrected LM relation, with each of the lines corresponding to a fit with the cumulative effect of these corrections taken into account. From the final fit to the mass corrected LM relation (Fig 5, red solid line), we find

Table 5. Observed scaling relations. Each scaling relation is fit with a power law relation of the form $E(z)^{\alpha}L_{\rm X} = A_0(X/X_0)^{\beta}$, where X_0 is 2 keV and $2{\times}10^{14}$ $M_{\odot}$ for kT and $M_{\rm X}$ respectively.

	Normalisation	Slope
$L_{\rm Xc} - kT_{\rm c}$	$A_{{\rm LT}_{\rm X,c}}(10^{43})$	$B_{{\rm LT}_{\rm X,c}}$
	2.4±0.5	2.6±0.7
$L_{\rm X,c} - M_{500,{\rm WL}}$	$A_{\rm LM}(10^{43})$	$B_{\rm LM}$
	1.9±0.2	1.33 (fixed)
Centroid Corrected		
$L_{\rm X,c} - M_{500,{\rm WL}}$	$A_{\rm LM}(10^{43})$	$B_{\rm LM}$
	2.2±0.3	1.33 (fixed)
Centroid and Edd. Bias Corrected		
$L_{\rm X,c} - M_{500,{\rm WL}}$	$A_{\rm LM}(10^{43})$	$B_{\rm LM}$
	2.9±0.5	1.33 (fixed)
Centroid, Edd. Bias and Ellipticity Corrected		
$L_{\rm X,c} - M_{500,{\rm WL}}$	$A_{\rm LM}(10^{43})$	$B_{\rm LM}$
	3.0±0.5	1.33 (fixed)
Centroid, Edd. Bias, Ellipticity and r_{500} Corrected		
$L_{\rm X,c} - M_{500,{\rm WL}}$	$A_{\rm LM,corr}(10^{43})$	$B_{\rm LM,corr}$
	5.6±0.9	1.33 (fixed)

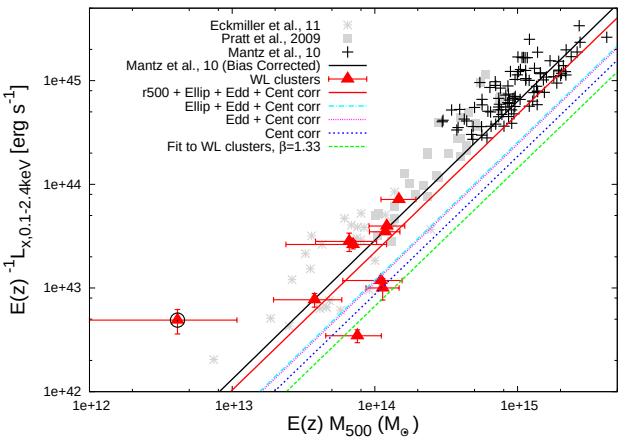

Figure 5. Figure showing the LM relation for the WL slected clusters (red triangles), with the WL masses corrected for centroid position (§ 5.1.1), Eddington bias (§ 5.1.2) and triaxiality (§ 5.1.3). Finally, the WL masses are derived within the X-ray determined r_{500} (see § 5.1.4). The cluster SLJ1634 is highlighted by the black circle. A power law fit for the LM relation with the masses corrected for these effects is given by the red solid line. Once again compared to the clusters given in Mantz et al. (2010b)(black crosses), and corresponding bias corrected LM relation (black line). The clusters from Pratt et al. (2009) and groups from Eckmiller, Hudson & Reiprich (2011) are also plotted, but shaded grey for clarity.

$A_{\rm LM,corr}$=(4.7±0.6)×10^{43} ergs s^{-1}, with the slope fixed at β=1.33. The comparison with the Mantz et al. (2010b) LM relation has been greatly reduced, and we find that the WL selected clusters are now consistent with X-ray selected clusters samples, albeit with three clusters being low luminosity outliers. We note that the clusters are only consistent when using WL masses derived within r^{X}_{500}, which may obscure the underlying discrepency. These corrections therefore show that clusters detected from WL surveys suffer from biases which have a large effect on the derived LM relation. By considering a series of plausible biases on the WL mass, the discrepancy in the LM relation, when compared to X-ray selected clusters, can be resolved.

5.2 Further Potential Mass Biases

In the following sections we discuss further biases which may have an effect when comparing WL and X-ray hydrostatic mass calculations.

5.2.1 WL Mass Bias due to Large-Scale Structure

It has been shown that correlated and uncorrelated large-scale structure (LSS) along the LOS, can both induce bias and scatter in the WL mass (e.g Metzler et al. 1999; Hoekstra 2001; White & Vale 2004; de Putter & White 2005; Noh & Cohn 2011; Becker & Kravtsov 2011). We should also note that the effects of LSS and triaxiality are related, where it can be considered that the major axis of halos is correlated with filamentary LSS (e.g. Splinter et al. 1997; Faltenbacher et al. 2002; Hopkins, Bahcall & Bode 2005; Lee & Evrard 2007; Zhang et al. 2009; Noh & Cohn 2011). The distribution of BCG ellipticities suggests that 60% of our clusters are viewed with the major axis close to the LOS, from which we can assume that they will also be affected by LSS along the LOS. However, Meneghetti et al. (2010) note that since they consider all the mass within 20 h^{-1}Mpc in their lensing simulations, the effect of correlated LSS is partially included in their estimate of the lensing mass. Therefore, the correction applied to our WL masses in Section 5.1.3 based upon Meneghetti et al. (2010), should partially include corrections for LSS. The effect of uncorrelated LSS has been found to not bias the WL mass, but adds additional scatter ≈15-30% as a function of cluster mass (Hoekstra et al. 2011; Becker & Kravtsov 2011).

5.2.2 Underestimates of X-ray Hydrostatic Mass

Simulations have shown that hydrostatic mass estimates of galaxy clusters are systematically biased towards underestimates of the true mass (e.g. Rasia, Tormen & Moscardini 2004; Kay et al. 2004; Nagai, Vikhlinin & Kravtsov 2007). Since hydrostatic estimates only take into account thermal pressure, the presence of additional pressure from random gas motions are neglected, and hence bias the mass low. It has been shown from simulations that up to ≈5%-20% of pressure support comes from random gas motions (e.g. Rasia et al. 2006; Lau, Kravtsov & Nagai 2009). However, the picture from observations is unclear. A recent study of 22 clusters detected by *Planck*, found that the average X-ray hydrostatic masses were 0.688±0.072 times lower than the masses determined from WL (von der Linden et al. 2014). Since the masses of the Mantz et al. (2010b) clusters are derived from a relation based upon X-ray hydrostatic mass estimates, in principle we can assume that their cluster masses are underestimated at the 10s% level.

As stated in Section 4.2, the masses in Mantz et al.

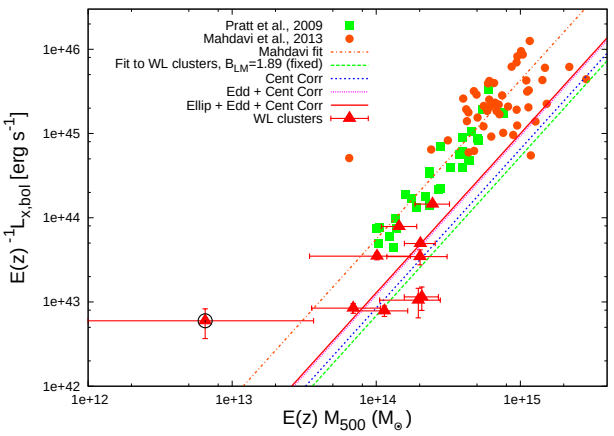

Figure 6. Figure showing the LM relation for the WL selected clusters (red triangles), with the WL masses corrected for centroid position (§ 5.1.1), Eddington bias (§ 5.1.2) and triaxiality (§ 5.1.3). The cluster SLJ1634 is highlighted by the black circle. A power law fit for the LM relation with the masses corrected for these effects is given by the red solid line. Also plotted are the Mahdavi et al. (2013, brown circles) clusters with WL masses in $r_{500}^{\rm WL}$. For reference, the Pratt et al. (2009, green squares) clusters are plotted, however these are X-ray mass estimates.

(2010b) are derived from the gas mass. They note that they incorporate a systematic fractional bias at r_{500} of 0.0325±0.06 on the gas mass measurements, based upon the simulations of Nagai, Vikhlinin & Kravtsov (2007). Therefore, this bias will be incorporated in the LM relation comparison. However, as our clusters probe a lower mass distribution than the Mantz et al. (2010b) sample (all M_{500} >3×10$^{14}M_{\odot}$), could the offset be explained by an increasing hydrostatic mass bias for lower cluster masses? The effect would be to not only lower the normalisation of the X-ray LM relation, but to also increase the slope, further decreasing the discrepancy of the LM relations. However, our comparison to the lower mass clusters of Pratt et al. (2009) and groups of Eckmiller, Hudson & Reiprich (2011) do not offer better agreement with our WL selected clusters. This has also been investigated based on simulations. Jeltema et al. (2008) showed that there is a weak correlation of mass underestimate with cluster mass, with low mass clusters (≈10^{14}M$_{\odot}$) having larger mass bias. Jeltema et al. (2008) find an underestimate of ∼20% at 10^{14}M$_{\odot}$. Recently, Israel et al. (2014) compared X-ray and WL cluster masses for a sample of 8 clusters in the 0.4≤z≤0.5 redshift range. They find a 1:1 correlation between the two mass estimates, but observe an intriguing mass bias at low WL masses at the ∼2σ level. However, other studies have found no hydrostatic mass bias as a function of mass (e.g. Lau, Kravtsov & Nagai 2009).

5.3 Comparison to X-ray Selected Cluster Sample with Weak Lensing Based Masses

We compare to the sample of clusters studied in Mahdavi et al. (2013), which is an X-ray selected cluster sample with WL derived cluster masses. The main advantage of choosing this sample is that the WL masses are derived within a WL determined r_{500}. As we have shown in Figure 5, the choice of r_{500} had the largest effect on the derived WL mass and may obscure any further underlying biases. By making this comparison we can remove the large effect of the choice of r_{500}. Furthermore, by comparing to WL masses the effects of hydrostatic mass bias (see § 5.2.2), and to a lesser extent the WL mass bias due to LSS (see § 5.2.1, but could still be larger in our sample compared to Mahdavi et al. (2013), due to the WL selection) will be reduced or removed.

Figure 6 plots the LM relation for our WL selected clusters (red triangles), and compared to the clusters studied in Mahdavi et al. (2013, brown circles)[5]. For the purposes of this comparison the X-ray luminosities are bolometric and in each case the WL masses are determined within a WL defined r_{500}. We fit a power law of the form $L_X = E(z)^2 L_0 (M/M_0)^{B_{\rm LM}}$ to the Mahdavi et al. (2013) clusters finding a normalisation of $L_{0,M13}$=(2.83±0.47)×10^{45}ergs s^{-1} and slope $B_{LM,M13}$=1.89±0.83, with M_0=8×10^{14}M$_{\odot}$. We fit to our WL clusters with the slope fixed at the value found for the Mahdavi et al. (2013) relation ($B_{LM,M13}$=1.89), and find a normalisation of L_0=(3.8±0.8)×10^{43}ergs s^{-1} (at M_0=2×10^{14}M$_{\odot}$, see red solid line Fig 6. Therefore, for a given mass we find that our WL selected clusters are 5.4±1.4 times under-luminous as compared to the Mahdavi et al. (2013) clusters in terms of the LM relation, with the masses derived from WL and within a WL determined r_{500} (corrected for centroid position, Eddington bias and triaxiality). Conversely, the masses are over-estimated by a factor 2.4±0.3 for a given luminosity. To validate that the X-ray selected clusters of Mahdavi et al. (2013), whose masses are derived from WL and within $r_{500}^{\rm WL}$, follow other X-ray selected clusters, we plot the Pratt et al. (2009) clusters (Fig 6, green squares). Clearly, the two X-ray selected samples are in agreement, even though the mass estimates are from two different methods, with our WL selected clusters offset from both samples. We note that if the Mahdavi et al. (2013) WL masses are calculated within an X-ray derived r_{500}, this has a negligible effect on their LM relation.

Since the discrepancy with the Mahdavi et al. (2013) sample is still prevalent (see Fig 6), even after correcting our WL masses for centroid position, Eddington bias and triaxiality, this implies that there is still some underlying effect due to the WL selection of these clusters.

5.4 Are WL Selected Clusters Under-luminous?

In Section 5.1 we have shown that by considering various systematic effects on the WL cluster mass, we are unable to reconcile the differences seen in the LM relation (see Figure 6), without including corrections for r$_{500}$ which we argue masks the true discrepancy (see § 5.3, Fig 6). Not only that, our previous work (Hamana et al. 2009, Figure 5) found that the WL mass is consistent with previous studies when compared to the velocity dispersion (σ_v). We reproduce this comparison using $M_{\rm WL,500}$ in Figure 7. We find that the WL clusters (red triangles) are consistent with the X-ray selected clusters studied in Hoekstra (2007, grey crosses), in terms of the $M_{\rm WL,500}$-σ_v relation. Therefore, we are presented with the situation that the WL mass and σ_v are consistent and

[5] The data were downloaded from http://sfstar.sfsu.edu/cccp/

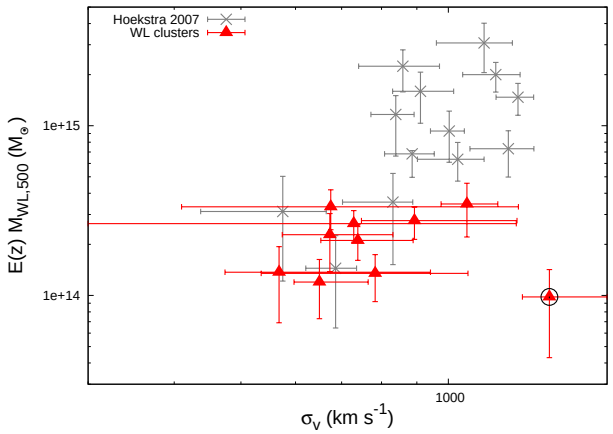

Figure 7. Figure showing the $M_{\rm WL,500}$-σ_v relation for the WL selected clusters (red triangles). The cluster SLJ1634 is highlighted by the black circle. The clusters studied in Hoekstra (2007) are plotted for comparison (grey crosses).

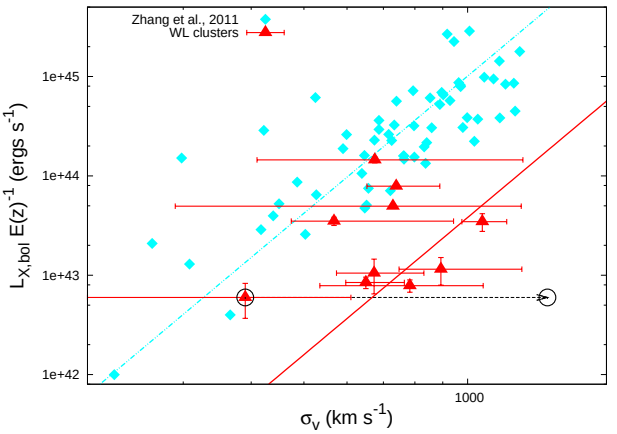

Figure 8. Figure showing the $L_{\rm X,bol}$-σ_v for the WL selected clusters (red triangles). The cluster SLJ1634 is highlighted by the black circle. The open black circle represents the estimate of the velocity dispersion for SLJ1634 from Hamana et al. (2009), when including all spectroscopic galaxies. The HIFLUGCS clusters studied in Zhang et al. (2011, cyan diamonds) is plotted for comparison.

the luminosity and temperature are consistent, implying the ICM properties are inconsistent with σ_v.

To quantify this, we derive a $L_{\rm X,bol}$-σ_v relation for the WL clusters. Figure 8 plots the $L_{\rm X,bol}$-σ_v relation for our clusters (red triangles), compared to the relation for the HIFLUGCS sample of clusters (cyan diamonds) studied in Zhang et al. (2011). The cluster SLJ1634 is highlighted by the black circle. Due to the composite nature of this cluster (see §3.3.5), the value of σ_v from Hamana et al. (2009, σ_v=1402^{+334}_{-121} km s^{-1}) is likely an overestimate. We therefore re-derive σ_v from our tree analysis using the galaxies from group B (see Fig A9, balck squares), as two of these galaxies are associated with the X-ray emission, finding σ_v=390±220 km s^{-1}. We find that five of the WL selected clusters are clearly under-luminous for their velocity dispersion.

These results imply that there is a strong systematic effect remaining that is influencing the WL and dynamical properties, the ICM properties, or both. We consider the most plausible effect to be a high incidence of projected filamentary structure along the LOS to these WL selected clusters, leading to enhanced WL masses and σ_v relative to halo mass. From the spectroscopic follow-up, many of the clusters show signs of non-gaussianity in their velocity dispersion histograms (see Fig 1 in Hamana et al. 2009), which would be consistent with projected filament structure. This however is based on relatively small numbers of spectra in each case (an average of 14 galaxies per cluster), so a more detailed analysis is unable to be performed.

Bower et al. (1997) investigated a sample of optically selected, X-ray under-luminous clusters and proposed two scenarios for their observed offset in the $L_{\rm X}$-σ_v relation. Either the clusters have not yet formed or are at a stage of rapid mass accretion, which would be manifested in a low X-ray luminosity. The second scenario is that the clusters are embedded in filaments viewed along the LOS, which would lead to an over-estimate of σ_v due to contamination of galaxies along the filament. Other previous studies looking at X-ray under-luminous clusters (e.g. Popesso et al. 2007; Balogh et al. 2011; Castellano et al. 2011) favour the scenario that these clusters are still in a stage of formation or that the gas has been expelled. However, since we have measured temperatures for the majority of our clusters and shown that the gas properties scale consistently in the luminosity-temperature relation (and consistent to X-ray selected cluster samples), we favour the scenario that the WL selected clusters are embedded in filaments viewed near the LOS. This is further corroborated by our measurements of the BCG ellipticity, where the majority of our cluster BCGs appear circular, implying that the WL selection strongly favours clusters elongated along the LOS and embedded in correlated filaments.

6 SUMMARY AND CONCLUSIONS

We have presented the results of X-ray observations of 10 WL selected galaxy clusters in order to determine their X-ray properties. Our main results are as follows.

(i) We find that the scaling relation between X-ray luminosity and temperature is consistent with samples of X-ray selected clusters.

(ii) We find that the WL selected clusters are offset from X-ray selected clusters and groups in the luminosity-temperature relation, implying either the X-ray luminosity is under-estimated or the WL mass is over-estimated.

(iii) The centroid shifts for the WL clusters show that the majority appears dynamically unrelaxed compared to X-ray selected samples, suggesting X-ray cluster surveys preferentially detect clusters that are morphologically relaxed and/or WL selection favours morphologically disturbed clusters.

(iv) The cuspiness of the gas density profiles shows that two of the clusters in our sample appear to host a cool core.

(v) Measuring the ellipticities of the BCGs for each cluster, and assuming that they are intrinsically prolate, we find that 60% of the clusters appear to be viewed with their major axis close to the line of sight.

(vi) Through a series of corrections to the WL cluster

mass including the centroid position, Eddington bias, and triaxiality, and calculating the WL masses with an X-ray derived r_{500}, we find the WL selected clusters are consistent in the LM relation with X-ray selected clusters.

(vii) Comparisons to X-ray selected samples with WL derived cluster masses, and within WL defined r_{500}s, show that the offset in the LM relation is still present, even when correcting for centroid position, Eddington bias, and triaxiality.

Our results show that WL selected clusters are affected by biases which, when combined, has a large effect on the calculated WL mass. We have presented a series of possible biases to explain the large offset of the LM relation when compared to X-ray selected cluster samples. When considering the cumulative effect of these biases on the WL mass we reconcile the difference in the LM relation. Our comparison to an X-ray selected sample of clusters with WL derived cluster masses, show that even after taking into account biases which may arise due to the WL selection, there is still a discrepancy in the LM relation. This implies that there maybe further biases in the WL selection, or that the WL selected clusters are embedded in filamentary structure viewed along the line of sight.

ACKNOWLEDGMENTS

We thank Massimo Meneghetti for providing data in electronic format of his simulated clusters. PAG also acknowledges support from the UK Science and Technology Facilities Council. RM is supported by a Royal Society University Research Fellowship, and European Research Council grant MIRG-CT-208994. This research made use of observations taken with *Chandra* awarded in proposal ID 12800522 (P.I. PAG), data from the *Chandra* data archive and data from the *XMM-Newton* data archive.

REFERENCES

Akritas M. G., Bershady M. A., 1996, ApJ, 470, 706
Arnaud M., Pointecouteau E., Pratt G. W., 2007, A&A, 474, L37
Bahé Y. M., McCarthy I. G., King L. J., 2012, MNRAS, 421, 1073
Balogh M. L., Mazzotta P., Bower R. G., Eke V., Bourdin H., Lu T., Theuns T., 2011, MNRAS, 412, 947
Becker M. R., Kravtsov A. V., 2011, ApJ, 740, 25
Birkinshaw M., 1999, Phys. Rep., 310, 97
Böhringer H. et al., 2004, A&A, 425, 367
—, 2007, A&A, 469, 363
Bower R. G., Castander F. J., Ellis R. S., Couch W. J., Boehringer H., 1997, MNRAS, 291, 353
Castellano M. et al., 2011, A&A, 530, A27
Coppin K. et al., 2006, MNRAS, 372, 1621
Corless V. L., King L. J., 2007, MNRAS, 380, 149
de Putter R., White M., 2005, 10, 676
Duffy A. R., Schaye J., Kay S. T., Dalla Vecchia C., 2008, MNRAS, 390, L64
Ebeling H., Edge A. C., Bohringer H., Allen S. W., Crawford C. S., Fabian A. C., Voges W., Huchra J. P., 1998, MNRAS, 301, 881
Ebeling H., Edge A. C., Mantz A., Barrett E., Henry J. P., Ma C. J., van Speybroeck L., 2010, MNRAS, 407, 83
Eckmiller H. J., Hudson D. S., Reiprich T. H., 2011, A&A, 535, A105
Faltenbacher A., Gottlöber S., Kerscher M., Müller V., 2002, A&A, 395, 1
Fasano G. et al., 2010, MNRAS, 404, 1490
Hamana T., Miyazaki S., Kashikawa N., Ellis R. S., Massey R. J., Refregier A., Taylor J. E., 2009, PASJ, 61, 833
Hoekstra H., 2001, A&A, 370, 743
—, 2007, MNRAS, 379, 317
Hoekstra H., Hartlap J., Hilbert S., van Uitert E., 2011, MNRAS, 412, 2095
Hoekstra H., Mahdavi A., Babul A., Bildfell C., 2012, MNRAS, 427, 1298
Hopkins P. F., Bahcall N. A., Bode P., 2005, ApJ, 618, 1
Hudson D. S., Mittal R., Reiprich T. H., Nulsen P. E. J., Andernach H., Sarazin C. L., 2010, A&A, 513, A37
Israel H., Erben T., Reiprich T. H., Vikhlinin A., Sarazin C. L., Schneider P., 2012, A&A, 546, A79
Israel, H., Reiprich, T. H., Erben, T., et al. 2014, arXiv:1402.3267
Jee M. J. et al., 2011, ApJ, 737, 59
Jeltema T. E., Hallman E. J., Burns J. O., Motl P. M., 2008, ApJ, 681, 167
Jing Y. P., Suto Y., 2002, ApJ, 574, 538
Kalberla P. M. W., Burton W. B., Hartmann D., Arnal E. M., Bajaja E., Morras R., Pöppel W. G. L., 2005, A&A, 440, 775
Kay S. T., Thomas P. A., Jenkins A., Pearce F. R., 2004, MNRAS, 355, 1091
Kravtsov A. V., Vikhlinin A., Nagai D., 2006, ApJ, 650, 128
Lau E. T., Kravtsov A. V., Nagai D., 2009, ApJ, 705, 1129
Lee J., Evrard A. E., 2007, ApJ, 657, 30
Mahdavi A., Hoekstra H., Babul A., Bildfell C., Jeltema T., Henry J. P., 2013, ApJ, 767, 116
Mantz A., Allen S. W., Ebeling H., Rapetti D., 2008, MNRAS, 387, 1179
Mantz A., Allen S. W., Ebeling H., Rapetti D., Drlica-Wagner A., 2010a, MNRAS, 406, 1773
Mantz A., Allen S. W., Rapetti D., Ebeling H., 2010b, MNRAS, 406, 1759
Markevitch M. et al., 2003, ApJ, 583, 70
Marrone D. P. et al., 2012, ApJ, 754, 119
Maughan B. J., 2007, ApJ, 668, 772
Maughan B. J., Giles P. A., Randall S. W., Jones C., Forman W. R., 2012, MNRAS, 421, 1583
Maughan B. J., Jones C., Forman W., Van Speybroeck L., 2008, ApJS, 174, 117
Meneghetti M., Rasia E., Merten J., Bellagamba F., Ettori S., Mazzotta P., Dolag K., Marri S., 2010, A&A, 514, A93
Metzler C. A., White M., Norman M., Loken C., 1999, ApJ, 520, L9
Miyazaki S., Hamana T., Ellis R. S., Kashikawa N., Massey R. J., Taylor J., Refregier A., 2007, ApJ, 669, 714
Nagai D., Vikhlinin A., Kravtsov A. V., 2007, ApJ, 655, 98
Noh Y., Cohn J. D., 2011, MNRAS, 413, 301
Oguri M., Hamana T., 2011, MNRAS, 414, 1851
Okabe N., Takada M., Umetsu K., Futamase T., Smith G. P., 2010a, PASJ, 62, 811
Okabe N., Zhang Y.-Y., Finoguenov A., Takada M., Smith

G. P., Umetsu K., Futamase T., 2010b, ApJ, 721, 875
Planck Collaboration et al., 2011a, A&A, 536, A8
—, 2011b, A&A, 536, A9
Poole G. B., Fardal M. A., Babul A., McCarthy I. G., Quinn T., Wadsley J., 2006, MNRAS, 373, 881
Popesso P., Biviano A., Böhringer H., Romaniello M., 2007, A&A, 461, 397
Pratt G. W., Croston J. H., Arnaud M., Böhringer H., 2009, A&A, 498, 361
Rasia E. et al., 2006, MNRAS, 369, 2013
Rasia E., Tormen G., Moscardini L., 2004, MNRAS, 351, 237
Santos J. S., Tozzi P., Rosati P., Böhringer H., 2010, A&A, 521, A64
Shan H. et al., 2012, ApJ, 748, 56
Shaw L. D., Weller J., Ostriker J. P., Bode P., 2006, ApJ, 646, 815
Smith R. K., Brickhouse N. S., Liedahl D. A., Raymond J. C., 2001, ApJ, 556, L91
Splinter R. J., Melott A. L., Linn A. M., Buck C., Tinker J., 1997, ApJ, 479, 632
Staniszewski Z. et al., 2009, ApJ, 701, 32
Vanderlinde K. et al., 2010, ApJ, 722, 1180
Vikhlinin A. et al., 2009a, ApJ, 692, 1033
Vikhlinin A., Kravtsov A., Forman W., Jones C., Markevitch M., Murray S. S., Van Speybroeck L., 2006, ApJ, 640, 691
Vikhlinin A. et al., 2009b, ApJ, 692, 1060
von der Linden, A., Mantz, A., Allen, S. W., et al. 2014, arXiv:1402.2670
Warren M. S., Quinn P. J., Salmon J. K., Zurek W. H., 1992, ApJ, 399, 405
White M., Vale C., 2004, Astroparticle Physics, 22, 19
Wittman D., Dell'Antonio I. P., Hughes J. P., Margoniner V. E., Tyson J. A., Cohen J. G., Norman D., 2006, ApJ, 643, 128
Zhang Y., Yang X., Faltenbacher A., Springel V., Lin W., Wang H., 2009, ApJ, 706, 747
Zhang Y.-Y., Andernach H., Caretta C. A., Reiprich T. H., Böhringer H., Puchwein E., Sijacki D., Girardi M., 2011, A&A, 526, A105

APPENDIX A: X-RAY AND *SUBARU* IMAGES OF INDIVIDUAL CLUSTERS

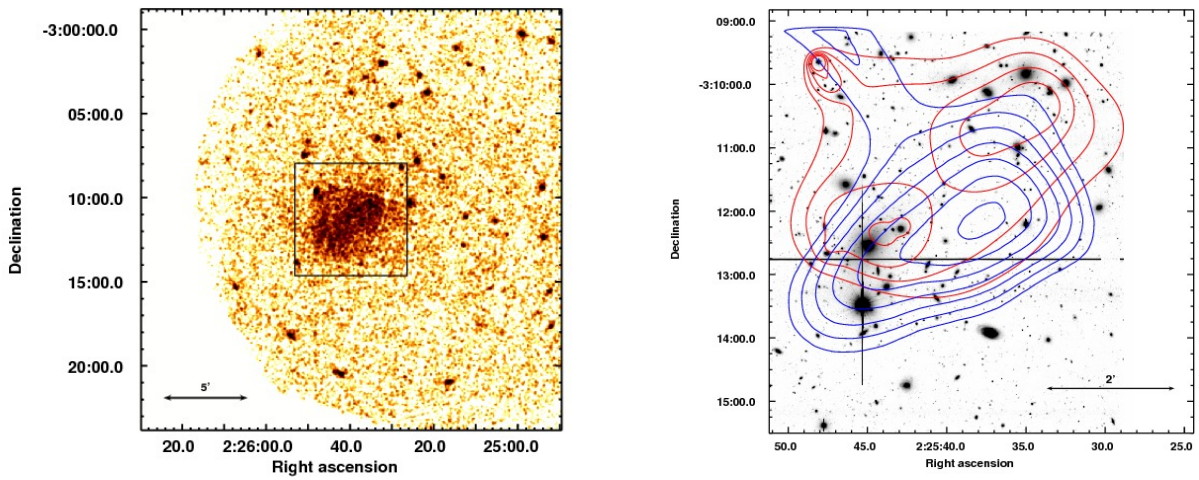

(a) (b)

Figure A1. Images for the cluster SLJ0225 (z=0.1395). Figure (a) shows the *XMM* image of the cluster in the 0.7 – 2.0 keV band smoothed by a Gaussian of 1.5 pixel radius (where 1 pixel = 2.2′); (b) shows a *Subaru* image of the cluster within a region 400×400″ in length (shown by the black box in Fig(a)) with X-ray contours (red) and WL mass contours (blue) over-plotted. The X-ray contours were constructed from an adaptively smoothed image of the total MOS data, due to the cluster falling on the chip gaps of the pn-camera. The WL contours are taken from Hamana et al. (2009).

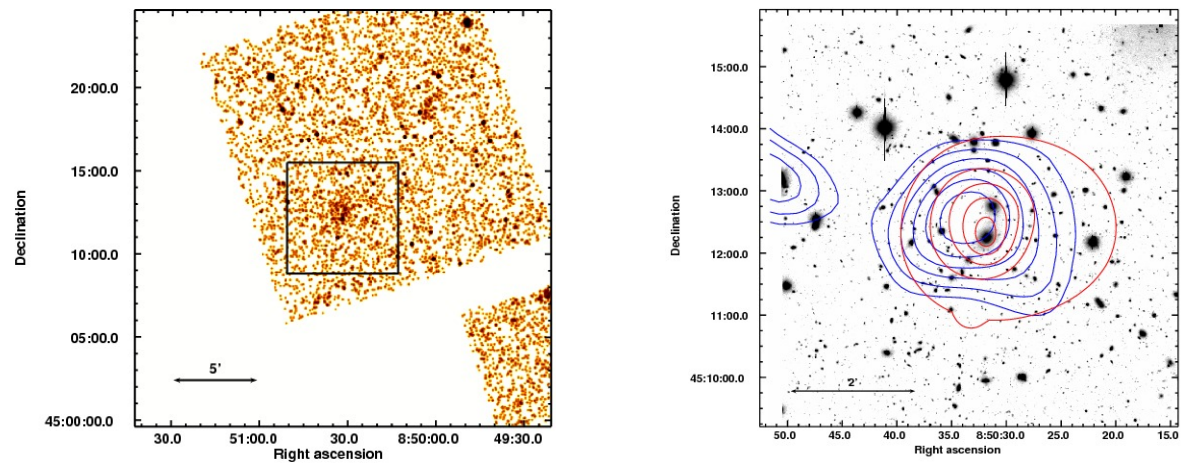

(a) (b)

Figure A2. Images for the cluster SLJ0850 (z=0.1938). (a) shows a *Chandra* image in the 0.7–2.0 keV band within a region 25×25′ in length, the image is smoothed by a Gaussian of 1.5 pixel radius (where 1 pixel = 1.968″); (b) shows a *Subaru* image of the cluster within a region 400×400″ in length (shown by the black box in Fig (a)) with the X-ray contours (red) and WL mass contours (blue) over-plotted. The X-ray contours were constructed from an adaptively smoothed *Chandra* image of the cluster.

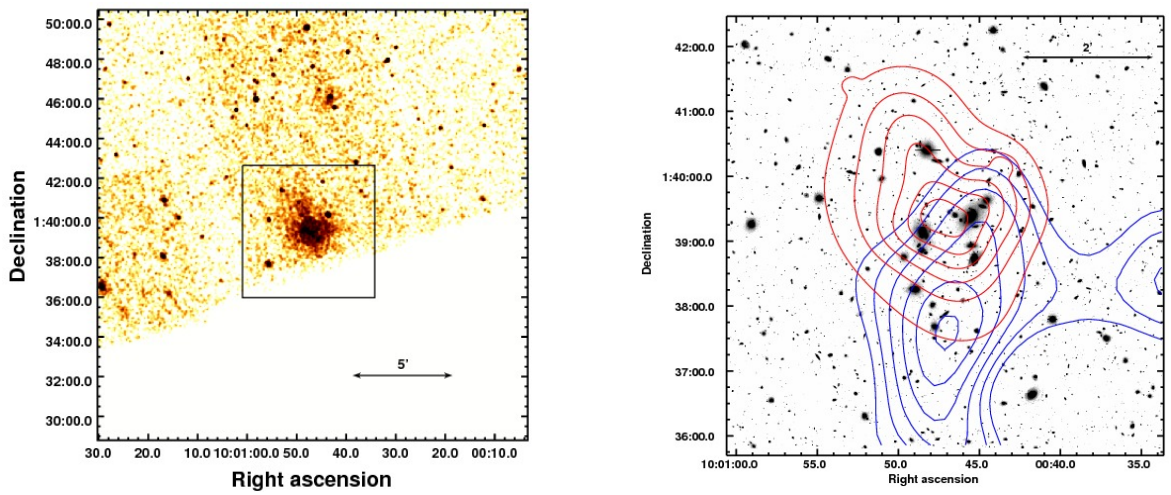

(a) (b)

Figure A3. Images for the cluster SLJ1000 (z=0.2166). Figures (a) and (b) same as A2.

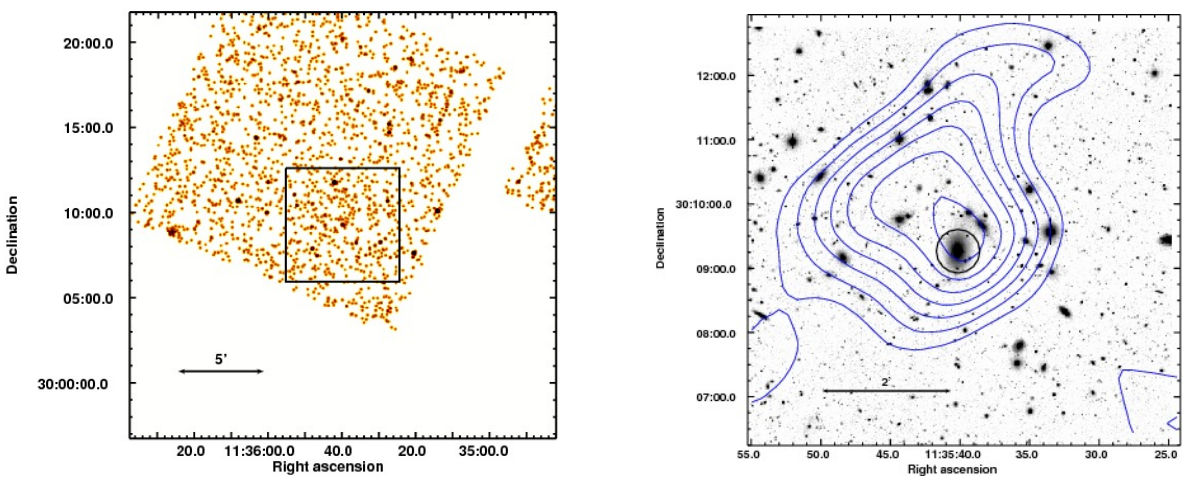

(a) (b)

Figure A4. Images for the cluster SLJ1135 (z=0.2078). Figures (a) and (b) same as A2, however due to the low SNR of this cluster an adaptively smoothed image of the cluster was not obtained.

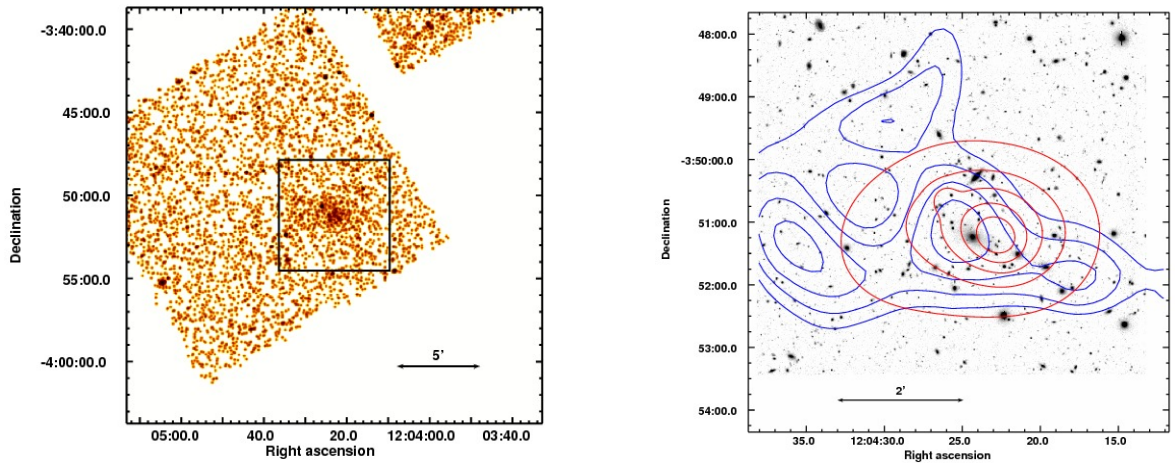

(a) (b)

Figure A5. Images for the cluster SLJ1204 (z=0.2609). Figures (a) and (b) same as A2.

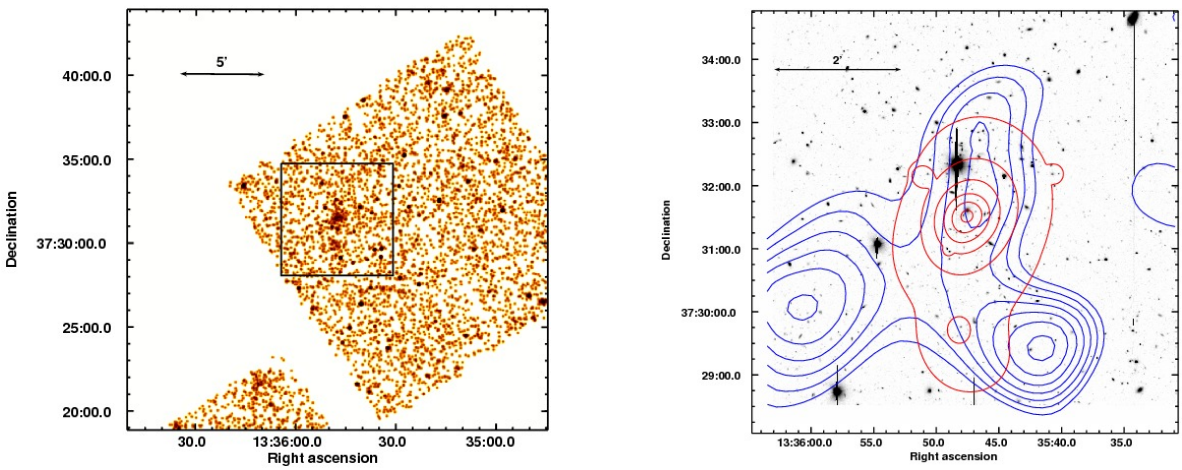

(a) (b)

Figure A6. Images for the cluster SLJ1335 (z=0.4070). Figures (a) and (b) same as A2.

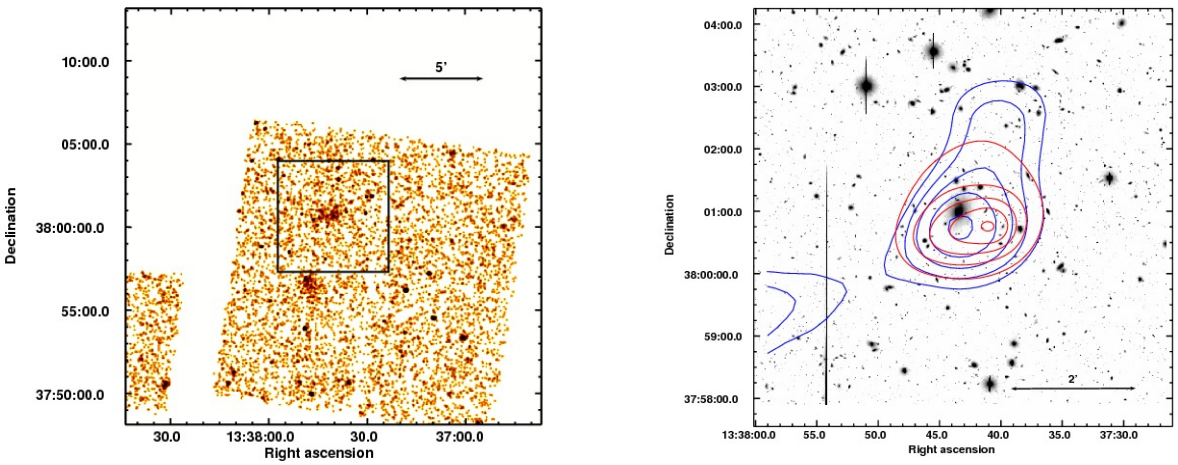

(a) (b)

Figure A7. Images for the cluster SLJ1337 (z=0.1798). Figures (a) and (b) same as A2.

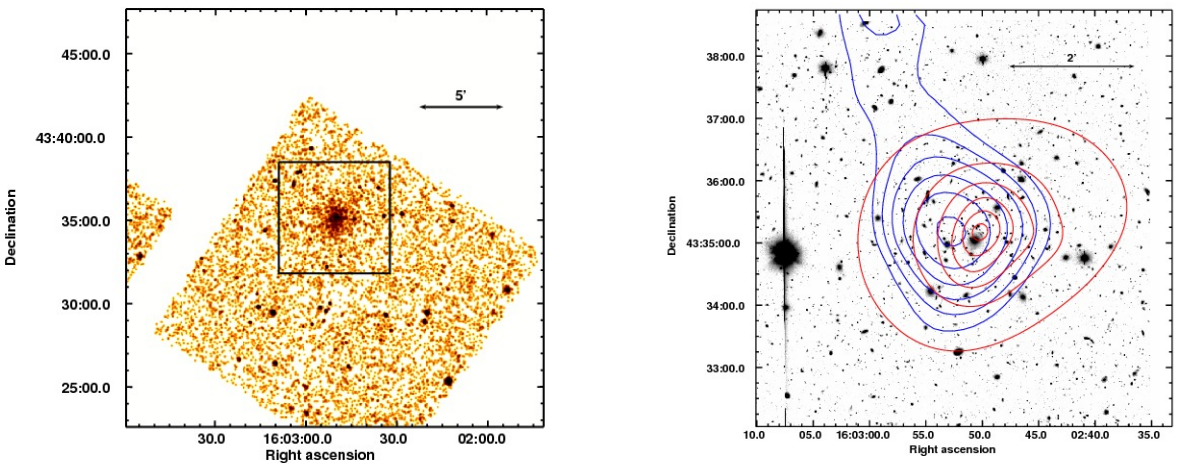

(a) (b)

Figure A8. Images for the cluster SLJ1602 (z=0.4155). Figures (a) and (b) same as A2.

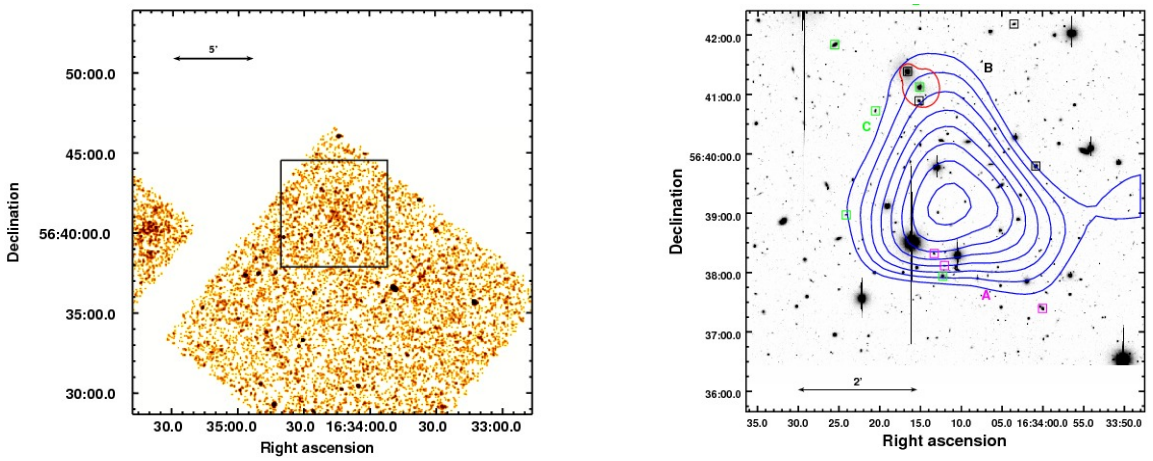

(a) (b)

Figure A9. Images for the cluster SLJ1634 (z=0.2377). Figures (a) and (b) same as A2. Also highlighted on Figure (b) is the locations of spectroscopically confirmed cluster galaxies, separated into three groups A, B and C (magenta, black and green squares respectively) found by our tree analysis (see § 3.3.5).

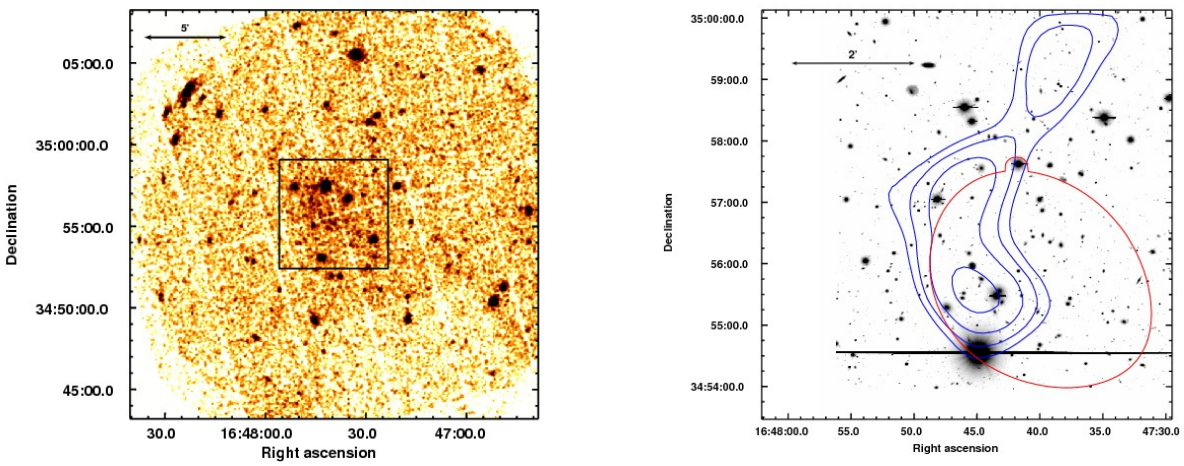

(a) (b)

Figure A10. Images for the cluster SLJ1647 (z=0.2592). Figures (a) and (b) same as A2.